

An analysis of satellite, radiosonde, and lidar observations of upper tropospheric water vapor from the Atmospheric Radiation Measurement Program

Brian J. Soden,¹ David D. Turner,² Barry M. Lesht,³ and Larry M. Miloshevich⁴

Received 2 June 2003; revised 29 October 2003; accepted 12 November 2003; published 25 February 2004.

[1] To improve our understanding of the distribution and radiative effects of water vapor, the U.S. Department of Energy Atmospheric Radiation Measurement (ARM) Program has conducted a series of coordinated water vapor Intensive Observation Periods (IOPs). This study uses observations collected from four ARM IOPs to accomplish two goals: First we compare radiosonde and Raman lidar observations of upper tropospheric water vapor with colocated geostationary satellite radiances at 6.7 μm . During all four IOPs we find excellent agreement between the satellite and Raman lidar observations of upper tropospheric humidity with systematic differences of $\sim 10\%$. In contrast, radiosondes equipped with Vaisala sensors are shown to be systematically drier in the upper troposphere by $\sim 40\%$ relative to both the lidar and satellite measurements. Second, we assess the performance of various “correction” strategies designed to rectify known deficiencies in the radiosonde measurements. It is shown that existing methods for correcting the radiosonde dry bias, while effective in the lower troposphere, offer little improvement in the upper troposphere. An alternative method based on variational assimilation of satellite radiances is presented and, when applied to the radiosonde measurements, is shown to significantly improve their agreement with coincident Raman lidar observations. It is suggested that a similar strategy could be used to improve the quality of the global historical record of radiosonde water vapor observations during the satellite era. *INDEX TERMS*: 3309 Meteorology and Atmospheric Dynamics: Climatology (1620); 3359 Meteorology and Atmospheric Dynamics: Radiative processes; 3360 Meteorology and Atmospheric Dynamics: Remote sensing; *KEYWORDS*: upper tropospheric water vapor, radiation, remote sensing

Citation: Soden, B. J., D. D. Turner, B. M. Lesht, and L. M. Miloshevich (2004), An analysis of satellite, radiosonde, and lidar observations of upper tropospheric water vapor from the Atmospheric Radiation Measurement Program, *J. Geophys. Res.*, 109, D04105, doi:10.1029/2003JD003828.

1. Introduction

[2] Water vapor is a key variable for climate studies. It is the dominant greenhouse gas and provides the largest known feedback mechanism for amplifying climate change. Water vapor in the upper troposphere is particularly important in this respect. Although it represents only a small fraction of the total vapor mass, upper tropospheric water vapor has a disproportionately large effect on the outgoing longwave radiation [Udelhofen and Hartmann, 1995; Schmetz *et al.*, 1995] and therefore on climate sensitivity. Model calculations suggest that nearly two-thirds of total

radiative feedback from water vapor is expected to originate from the upper troposphere [Held and Soden, 2000]. Furthermore, climate model projections suggest that the concentration of water vapor in the upper troposphere should increase by as much as 50% over the next half-century. This large amplification highlights the importance of upper tropospheric water vapor, both as a feedback mechanism and as a potential fingerprint of anthropogenic climate change, further underscoring the need for its accurate observation [Kley *et al.*, 2000] (available at <http://www.aero.jussieu.fr/~sparc>).

[3] Even though it plays a critical role in determining climate sensitivity, our ability to monitor changes in water vapor is lacking. This problem is most evident in the upper troposphere where the small concentrations of water vapor make accurate in situ measurement difficult [Kley *et al.*, 2000]. Because of their prolonged existence and wide geographic coverage, radiosondes provide an essential component of the global observing system. However, previous studies have documented substantial spatial [Soden and Lanzante, 1996] and temporal [Elliott and Gaffen, 1991; Free *et al.*, 2002] discontinuities in their historical records

¹Geophysical Fluid Dynamics Laboratory, National Oceanic and Atmospheric Administration, Princeton, New Jersey, USA.

²Cooperative Institute for Meteorological Satellite Studies, University of Wisconsin-Madison, Madison, Wisconsin, USA.

³Environmental Research Division, Argonne National Laboratory, Argonne, Illinois, USA.

⁴National Center for Atmospheric Research, Boulder, Colorado, USA.

that are frequently related to differences in radiosonde instrumentation. More recently, even subtler dependencies have been uncovered as systematic differences in radiosonde water vapor profiles have been linked to the age or “vintage” of the sensor and packaging materials used during storage of the sensor [Lesht, 1999; Guichard *et al.*, 2000; Miloshevich *et al.*, 2001; Turner *et al.*, 2003] (the former is available at http://www.arm.gov/docs/documents/technical/conf_9903/lesht-99.pdf).

[4] Despite these limitations, radiosondes are still widely used to provide water vapor profiles both for field campaigns and as part of national observing networks. As a result, considerable effort has been made to develop methods to correct for known deficiencies in their measurement. The Atmospheric Radiation Measurement (ARM) Program has conducted a series of water vapor Intensive Observation Periods (IOPs) designed to better understand our ability to measure tropospheric water vapor and its radiative effects [Revercomb *et al.*, 2003]. This study uses observations collected from four ARM IOPs to (1) evaluate the consistency of current radiosonde observations relative to both Raman lidar and satellite radiance observations and (2) assess the performance of various radiosonde “correction” strategies in the upper troposphere.

[5] Section 2 outlines the radiosonde, Raman lidar, and satellite data used in this study and briefly describes three different procedures that are currently used to rectify the radiosonde humidity profiles. In section 3 of this study, we compare radiosonde observations from both Vaisala RS80 and RS90 Humicap sensors with colocated Raman lidar and satellite measurements of upper tropospheric humidity (UTH). During all four IOPs, the radiosonde observations are found to be systematically drier in the upper troposphere relative to both the Raman lidar and satellite observations by as much as 40%. In contrast, the Raman lidar and satellite measurements obtained from the Geostationary Operational Environmental Satellite (GOES) are shown to agree with each other to within $\sim 10\%$. Finally, in section 4 we examine the impact of existing “correction” methods designed to rectify known deficiencies in the radiosonde humidity sensors. While useful for the lower troposphere, we show that these algorithms offer little improvement in the upper troposphere (between ~ 200 and 500 hPa). An alternative strategy, based on variational assimilation of satellite radiances, is proposed and, when applied to the radiosonde measurements, is shown to significantly improve their agreement with coincident Raman lidar observations.

2. Data and Analysis Procedure

2.1. Radiosonde Soundings

[6] The primary radiosonde used during the ARM IOPs was the Vaisala model RS80-H. The humidity sensor in the RS80-H is based on a polymer membrane that acts as the dielectric in a thin-film capacitor. Water molecules bound to the polymer change its dielectric value and hence the capacitance, which is the fundamental variable sensed. The polymer surface is intended to mimic the behavior of a water surface with respect to adsorption of ambient water vapor. Because the polymer’s water vapor adsorption capacity depends on its temperature, the sensor responds to

changes in relative humidity (RH) rather than to changes in absolute humidity. Relative humidity measured by Vaisala radiosondes are always reported as RH (%) with respect to water.

[7] A considerable amount of evidence has been accumulated showing that humidity measurements from the Vaisala RS80 radiosonde (both the H variety and the older A variety) exhibit a dry bias in both the lower and upper troposphere [Soden *et al.*, 1994; Ferrare *et al.*, 1995; Soden and Lanzante, 1996; Lesht and Liljegren, 1997; Lesht, 1999; Lesht and Richardson, 2002; Ross and Gaffen, 1998; Turner and Goldsmith, 1999; Richardson *et al.*, 2000; Kley *et al.*, 2000; Miloshevich *et al.*, 2001; Turner *et al.*, 2003]. Investigation by Vaisala suggests that contamination of the polymer membrane by organic molecules that originate in the radiosonde packaging is the major cause of the lower tropospheric dry bias [Wang *et al.*, 2002]. The radiosonde RH values tend to be low because the organic contaminants occupy binding sites that otherwise might be available to water molecules. The amount of contamination seems to depend on the radiosonde age and has a larger effect at high values of RH. In addition to the contamination problem, additional sources of bias resulting from sensor calibration errors and time lag effects have also been documented [Miloshevich *et al.*, 2003] (available at <http://www.arm.gov/docs/documents/technical/conference.html>). As a result, three different correction methods (outlined below) have been developed in an attempt to rectify these deficiencies.

[8] Finally, a new radiosonde, called the RS90, is now being manufactured by Vaisala. The RS90 is similar to the RS80-H described above, but is better calibrated and has an improved design which decreases the sensor response time and reduces the impact of icing on in-cloud water vapor measurements [Miloshevich *et al.*, 2003]. Changes to the packaging material also reduce sensor contamination errors that have hampered the RS80-H observations. The ARM program launched several dozen of these radiosondes during the 2000 IOP in addition to the standard RS80-H launches. This paper will examine the impact that this change in radiosonde sensor has on the humidity profiles in the upper troposphere.

2.1.1. Vaisala Correction Method

[9] Vaisala and their colleagues at NCAR performed a set of experiments to understand and quantify the sources of RH measurement error in the RS80 sensor [Wang *et al.*, 2002]. Using data from the TOGA-COARE and other experiments, Wang *et al.* [2002] describe six different sources of error in RH measurements and present empirically based methods for correcting archived radiosonde data for these errors. Identical algorithms that treat the three most significant sources of error were provided to us during the course of our research [Lesht, 1999], and we used these to correct the ARM radiosonde data presented here. The three sources of error we addressed are the contamination error described above and two errors that result from the imprecision of the sensor calibration process.

2.1.1.1. Calibration Model Error

[10] The basic RS80 calibration model, or the function relating capacitance to RH at a fixed temperature, has some limitations. By performing detailed chamber tests on 400 radiosondes Vaisala concluded that the RH-80H cali-

bration model is inaccurate at high values of RH, tending to be too moist. They proposed a correction equation in the form of a third-order polynomial,

$$\Delta Um = H_0 + H_1U + H_2U^2 + H_3U^3, \quad (1)$$

in which ΔUm is the difference between a reference sensor value of RH and the radiosonde-reported RH value, U is the radiosonde reported RH value (adjusted to calibration temperature), and the H_i are empirical coefficients (numerical values are given by Wang *et al.* [2002]). The basic model error is insignificant through most of the RH range, but approaches 3% RH at the upper end of the scale. It should be noted that Wang *et al.* [2002], citing a procedural concern about the experiment from which equation (1) was derived (a concern not shared by their Vaisala colleagues), do not apply this correction. We do, however, include this correction in the results shown here.

2.1.1.2. Temperature Model Error

[11] Vaisala accounts for the sensitivity of the RH sensor to temperature by using another polynomial function that relates the output value of RH to the ambient temperature (t) and to the value of RH at calibration temperature (U) corresponding to the measured capacitance (equation (1)). Written as

$$RH = \frac{U + a_0 + a_1t + a_2t^2 + a_3t^3 + a_4t^4}{b_0 + b_1t + b_2t^2 + b_3t^3 + b_4t^4}, \quad (2)$$

a_i and b_i again are empirical coefficients. During chamber testing Vaisala determined that the original coefficient values used in equation (2) resulted in a dry bias at ice saturation levels. Vaisala derived an updated set of coefficients (presented by Wang *et al.* [2002]) that we used in our correction procedure as well.

2.1.1.3. Contamination Error

[12] The largest contribution to the lower tropospheric dry bias in the RS80-H radiosonde humidity measurements is that caused by contamination of the polymer sensor by organic molecules originating in the radiosonde's plastic parts. Vaisala has developed another polynomial function to describe the correction necessary to account for the contamination. Denoting C_{ch} as the correction (in % RH) to the relative humidity at calibration temperature (U), d as the age of the radiosonde in years, and kh_i and ph_i empirical constants, this function is written

$$C_{ch} = (kh_0 + kh_1d + kh_2d^2 + kh_3d^3 + kh_4d^4) * (ph_0 + ph_1U + ph_2U^2 + ph_3U^3). \quad (3)$$

Depending on the radiosonde age and the ambient temperature, this correction can approach 10% at high values of RH [e.g., Lesht, 1999, Figure 2]. While the sign of the correction is well established, its magnitude is still viewed to be highly uncertain because the corrections were derived empirically using a small data set with large unquantifiable variability [Miloshevich *et al.*, 2003]. Thus, of the three Vaisala corrections described here, the contamination correction is by far the most uncertain. For radiosondes produced after 1 June 2000, Vaisala has attempted to ameliorate the contamination problem by

placing a protective cap over the sensor (which is removed prior to launch). However, this change does not affect any of the RS80-H radiosondes used here, which were all manufactured before June 2000.

2.1.2. Empirical Scaling of Column-Integrated Water Vapor

[13] In addition to the radiosonde sensors, the ARM observation sites also rely on microwave radiometers (MWR) to provide accurate measurements of total column water vapor. One of the early methods for improving the quality of the Vaisala radiosonde moisture profiles relied on an empirical scaling of the radiosonde total column water vapor to match that retrieved from the MWR [Turner *et al.*, 2003]. For this correction, the mixing ratio at each level k is scaled by the ratio of the MWR to radiosonde total column water vapor,

$$\hat{q}_k = q_k \frac{W}{\frac{1}{g} \sum q_k \Delta p_k}, \quad (4)$$

where W is the observed precipitable water vapor from the MWR, q_k is the original radiosonde water vapor mixing ratio, and \hat{q}_k is the scaled water vapor mixing ratio. Note that this method implicitly assumes that the relative error in mixing ratio is invariant with height. If the relative error increases with height, as has been suggested by Miloshevich *et al.* [2003], this method will tend to underestimate the adjustments required in the upper troposphere.

2.1.3. Time Lag/Bias Correction Algorithm

[14] In addition to the bias errors described above, the radiosonde measurements are affected by a time lag error that results from slow sensor response to changes in the ambient RH at low temperatures. The time constant increases with decreasing temperature and exceeds one minute for temperatures below -45°C for the RS80-H sensor, and below -60°C for the faster RS90 sensor. Miloshevich *et al.* [2003] developed a correction algorithm for time lag error that calculates the ambient ("true") humidity profile from the measured humidity and temperature profiles, based on laboratory measurements of the sensor time constant as a function of temperature. The time lag correction recovers vertical structure in the RH profile that is "smoothed" by the slow sensor response at cold temperatures. The magnitude and sign of the correction varies according to the vertical humidity and temperature structure of a given profile, because it is sensitive to the local humidity gradient as well as the temperature. The time lag, temperature dependence, and contamination corrections were combined and applied to the ARM IOP measurements. The corrections increased the water vapor amount by a mean of 10% in the lower troposphere, increasing with height to 50–100% near the tropopause (depending on the IOP), with considerable variability about the mean.

[15] The time lag/bias correction algorithm has been evaluated by comparing 40 RH profiles measured simultaneously by RS80-H radiosondes and the reference-quality NOAA/CMDL cryogenic hygrometer [Miloshevich *et al.*, 2003]. The corrections reduced the mean dry bias relative to the hygrometer from 4% RH at -20°C and 10% RH at -70°C to $\pm 2\%$ RH at all temperatures. However, the standard deviation of about 4% RH indicates considerable

variability remaining in the corrected data, which is attributed to the large uncertainty in the contamination correction. The study revealed shortcomings in the contamination correction, which are mitigated by specifying a constant age of 1 year for all radiosondes when calculating the age-dependence portion of the contamination correction. The contamination issue was alleviated for radiosondes produced after 1 June 2000 by the introduction of a sealed sensor cap that is removed prior to launch.

2.2. Raman Lidar

[16] The Raman lidar was designed to be an operational instrument to profile water vapor, aerosol, and clouds throughout the diurnal cycle [Goldsmith *et al.*, 1998]. It transmits pulses of 355 nm laser light vertically into the atmosphere using a frequency tripled Nd:YAG laser operating at 30 Hz. The average energy of these pulses is approximately 350 mJ. The outgoing laser beam is expanded to reduce the laser beam divergence to 0.1 mrad, thereby permitting the use of a narrow field-of-view (~ 0.3 mrad). This narrow field-of-view, together with narrowband (~ 0.4 nm band pass) interference filters, enables the system to profile water vapor and aerosols continuously throughout the diurnal cycle by rejecting the out-of-scene and out-of-band solar radiation.

[17] The backscattered light is collected by a 61-cm telescope and the contributions from the Rayleigh-Mie scattering at the laser wavelength and the backscatter associated with the Raman shifted wavelengths of water vapor (408 nm) and nitrogen (387 nm) are directed toward photomultiplier tubes which operate in photon counting mode. The raw data are collected in 0.26 ms bins, which correspond to 39 m vertical resolution, and are stored at 1 min intervals (the accumulation of roughly 1740 shots). Often, the vertical and/or temporal resolution is degraded during post-processing to improve the signal-to-noise ratio. For the upper tropospheric measurements presented in this paper, the vertical resolution has been degraded to 312 m resolution, and the temporal resolution is 30 min. Goldsmith *et al.* [1998] provide a more complete description of this lidar system.

[18] The ratio of the Raman water vapor signal and the Raman nitrogen signal is, after a few corrections, proportional to the water vapor mixing ratio. The details of these corrections for this system are outlined by Turner and Goldsmith [1999]. However, the uncertainties in the ratio of the Raman cross sections of water vapor and nitrogen are on the order of 10% [Penney and Lapp, 1976]; therefore the corrected ratio of the Raman water vapor signal to the Raman nitrogen signal is typically calibrated using a height-independent calibration constant derived from another independent measure of water vapor. The lidar's water vapor mixing ratio profile is calibrated by adjusting the calibration value to achieve agreement in total precipitable water vapor with that retrieved from a colocated microwave radiometer [Turner *et al.*, 2002]. The calibration of the microwave radiometer is maintained by an automated algorithm that reduces the TIP-curve data when the sky is determined to be clear [Liljegren, 2000].

2.3. GOES Water Vapor Radiances

[19] We use radiance measurements in the 6.7 μm water vapor channel from the Geostationary Operational Environ-

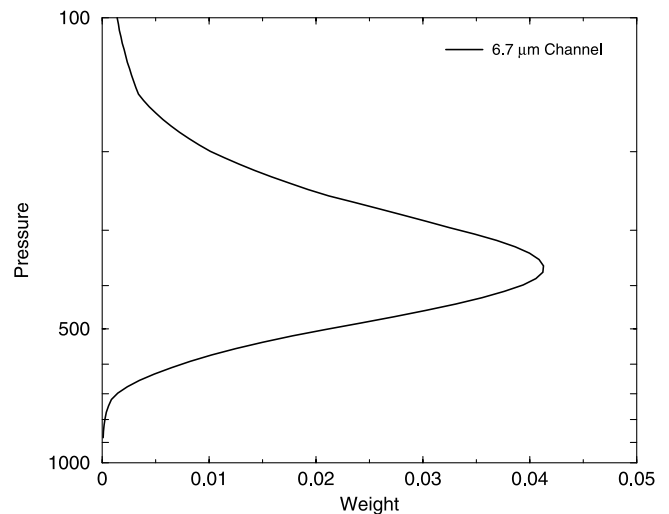


Figure 1. A typical GOES 6.7 μm weighting function for the ARM/SGP central facility. The weights were computed using the time-average temperature profile from the 2000 IOP, a constant relative humidity of 30%, and a satellite zenith angle of 48.49° , which corresponds to the viewing angle for the SGP central facility from GOES 8. The weights are normalized such that their sum over pressure equals unity.

mental Satellite (GOES 8) to provide a common benchmark for intercomparison with the ARM measurements of upper tropospheric water vapor. The high space (4 km) and time (30 min) sampling of the geostationary radiances facilitates their collocation with both in situ and surface based measurements. The 6.7 μm channel is located near the center of a strong water vapor absorption band and under clear skies is primarily sensitive to the relative humidity averaged over a deep layer centered in the upper troposphere. The weighting function for the 6.7 μm channel typically peaks between 200 and 500 hPa (Figure 1), although the location of this layer shifts depending upon the nature of the temperature and moisture profile under consideration as well as the satellite zenith angle. A detailed discussion of the sensitivity and interpretation of radiance observations in the 6.7 μm channel is provided by Soden and Bretherton [1993]. The noise equivalent delta-temperature (NEDT) for the 6.7 μm channel of GOES 8 is estimated to be ~ 0.2 K [Menzel *et al.*, 1998].

[20] Although observations of the 6.7 μm radiances have been available for nearly two decades, their quantitative use is often hindered by the difficulty of interpreting the observed radiances in terms of a more familiar water vapor quantity. Soden and Bretherton [1993] addressed this problem by deriving an analytic expression, based upon simplified radiative theory, for relating the 6.7 μm radiances to a layer-averaged relative humidity. Rather than attempting retrievals in the form of a vertical sounding, attention is focused on the information actually present in the radiances, minimizing extraneous assumptions. This analytical relationship, hereafter called a radiance-to-humidity transformation, provides a convenient means of interpreting the clear-sky 6.7 μm radiances in terms of a more familiar water

Table 1. Names, Dates, and Instrumentation Used From the Four ARM Intensive Observation Periods (IOPs)

IOP Name	Dates	Instrumentation
1996 water vapor IOP	10–30 Sept. 1996	GOES 8, Raman lidar, Vaisala RS80-H
1997 water vapor IOP	15 Sept. to 5 Oct. 1997	GOES 8, Raman lidar, Vaisala RS80-H
1999 lidar IOP	23 Sept. to 22 Oct. 1999	GOES 8, Raman lidar, Vaisala RS80-H
2000 water vapor IOP	17 Sept. to 8 Oct. 2000	GOES 8, Raman lidar, Vaisala RS80-H and RS90

vapor quantity and has been widely applied to the interpretation of multispectral satellite radiances in both the infrared [Stephens *et al.*, 1996; Slingo and Webb, 1997; Moody *et al.*, 1999; Bates and Jackson, 2001; Schmetz *et al.*, 1995] and microwave [Spencer and Braswell, 1997; Engelen and Stephens, 1998] portions of the spectrum.

[21] Following Goody [1964], each narrow, irregularly spaced line is assumed to behave as an independent, isolated absorber and the assemblage is then modeled as a large number of randomly located, overlapping lines. Using this random strong line theory, the brightness temperature ($T_{6.7}$) may be related to a vertically weighted average of the upper tropospheric relative humidity (UTH) according to

$$\ln\left(\frac{UTH \cdot p_0}{\cos \theta}\right) = a + b \cdot T_{6.7}, \quad (5)$$

where UTH is a layer-mean relative humidity weighted according to the sensitivity of the 6.7 μm channel (e.g., Figure 1), θ is the satellite zenith angle, $p_0 = p(T = T_{6.7})/300$ mb represents a normalized reference pressure for the channel, and $a = 31.5$ and $b = -0.115 \text{ K}^{-1}$ are linear coefficients tuned to replicate detailed radiative transfer calculations. For further details regarding the retrieval and sensitivity analysis, the reader is referred to Soden and Bretherton [1993], Soden *et al.* [1994], and Soden [1998].

[22] Since clouds strongly attenuate the emission of infrared radiation, estimation of the relative humidity requires information from pixels in which the $T_{6.7}$ is not affected by cloud cover. Given the vertical distribution of the 6.7 μm weighting function, this restriction usually corresponds to the exclusion of pixels containing middle and upper level clouds [Schmetz and Turpeinen, 1988]. Clear-sky $T_{6.7}$ is determined using the bi-spectral cloud masking scheme described by Soden [1998]. This procedure estimates the cloud top temperature from the 11 μm channel and uses the difference in brightness temperatures between the 11 μm and 6.7 μm channels ($\Delta T_b = T_{11} - T_{6.7}$) as a threshold to discriminate between clear and cloudy pixels. Pixels for which $\Delta T_b < 25$ K are considered to be cloud contaminated. This threshold is based upon theoretical calculations of the effect of clouds on the 6.7 μm radiance as well as sensitivity calculations [Soden and Bretherton, 1993; Soden, 1998]. The conclusions drawn below are insensitive to reasonable changes in this threshold. For example, changing the ΔT_b threshold from 25 K to 30 K changes the mean clear-sky $T_{6.7}$ from GOES by <0.5 K.

2.4. Comparison Procedure

[23] To compare the radiosonde and lidar measurements with the GOES observations, we follow a 2-step forward-modeling approach. In the first step, the measured profiles of water vapor and temperature are inserted into a narrow-band radiative transfer model to simulate the radiance that

would be observed by the satellite under those atmospheric conditions. The model used here is the HIRS Fast Forward Program (HFFP) which has been shown to agree with line-by-line calculations to within 0.1 K [Soden *et al.*, 2000]. Since the lidar provides moisture profiles only, temperature profiles are interpolated to the lidar observation times from the nearest adjacent radiosonde launches. The use of the same temperature information for both the lidar and radiosonde comparison insures that differences in $T_{6.7}$ between the two instruments stem solely from differences in their respective moisture profiles.

[24] The second step transforms both the GOES-observed and profile-simulated radiances into an upper tropospheric relative humidity (UTH) using equation (1). This approach has the advantage of providing both an accurate radiance-level comparison that eliminates uncertainties associated with retrieval algorithms, as well as providing a means of readily interpreting the radiance results in terms of a more familiar water vapor quantity. Because the translation to UTH is done in an identical manner for both the GOES-observed and profile-simulated radiance, it does not introduce spurious errors between the two UTH quantities.

[25] When calculating the simulated radiances, the water vapor retrievals from the Raman lidar are only used for those levels where the signal-to-noise ratio is less than 25%. This typically results in discarding the humidity information above ~ 200 mb. However, the radiative transfer calculations require moisture profiles to be specified up to an altitude of 100 mb. Therefore, to complete to moisture profile, the lidar humidity retrievals are extrapolated up to 100 mb by assuming a constant relative humidity equal to that found in the highest valid level in the lidar retrieval. The precise impact of this filling procedure is difficult to estimate. SAGE II climatologies of water vapor for 20–40 N [Chiou *et al.*, 1997] indicate that the relative humidity between 100–300 mb is very nearly constant, with the climatological humidity lapse rate varying from $+2\%/km$ to $-3\%/km$ depending upon the season. However, because the $T_{6.7}$ is relatively insensitive to levels above 200 mb (Figure 1), using even the largest of the SAGE humidity lapse rates in place of the constant relative humidity assumption used here alters the mean lidar UTH by less than 1%.

[26] By neglecting variations in p_0 , which are small relative to the magnitude of humidity variations, the differential form of equation (5) can be approximated as

$$\Delta \ln UTH \approx b \cdot \Delta T_{6.7}. \quad (6)$$

This provides a useful scaling relationship to translate errors in $T_{6.7}$ into relative errors in humidity. Each 1 K error in $T_{6.7}$ is equivalent to a fractional error in UTH of $b \cong -0.1$ (i.e., a percentage error of $\cong 10\%$). Recall that b is negative,

indicating that a warm (positive) bias in $T_{6.7}$ is associated with a dry (negative) bias in UTH.

3. Comparison Results

[27] This study presents results obtained from four water vapor IOPs conducted during the months of September–October 1996, 1997, 1999, and 2000. The dates of each IOP are listed in Table 1.

3.1. Radiosonde Versus GOES

[28] Figure 2 compares the time series of $T_{6.7}$ from the GOES pixel (solid line) that is located closest to the ARM central facility (36.609°N latitude, 97.485°W longitude) with the $T_{6.7}$ computed from the original (i.e., uncorrected) radiosonde humidity and temperature profiles (solid circles) launched from the central facility. Results are shown for all four IOPs: 1996 (Figure 2a), 1997 (Figure 2b), 1999 (Figure 2c), and 2000 (Figure 2d). On the right-hand side of each graph is the corresponding UTH scale derived from equation (1) assuming a constant value of $p_0 = 1.1$. Because the UTH increases exponentially with decreasing $T_{6.7}$, the brightness temperature scale is inverted so that cold (moist) $T_{6.7}$ is at the top of the graph and warm (dry) $T_{6.7}$ is at the bottom. Shaded regions indicate times where the GOES radiances are believed to be contaminated by cloud cover according to the cloud-screening mask described in section 2.4.

[29] The near-continuous record of GOES radiances illustrates the high degree of variability in upper tropospheric moisture. The humidity conditions inferred from GOES span a large dynamic range, with $T_{6.7}$ ranging from values as cold (moist) as ~ 230 K ($\sim 100\%$ UTH) to values as warm (dry) as ~ 255 K ($\sim 8\%$ UTH). The occasional supersaturated values of UTH may indicate periods of thin cirrus that were not detected by the cloud-screening algorithm, or they may indicate true supersaturated conditions (with respect to ice), which have been observed in the upper troposphere [Heymsfield *et al.*, 1998].

[30] Comparison of the time series of GOES and radiosonde observations (Figure 2) reveals a similar temporal evolution in UTH between the two instruments. This similarity is, by itself, noteworthy given the concerns regarding the quality of radiosonde humidity observations in the upper troposphere. However, despite the similar variability between the two measurements, the radiosondes clearly exhibit a substantial dry bias relative to the GOES observations. This bias is quite robust, occurring in virtually every radiosonde sounding of all four IOPs, and is qualitatively consistent with the dry bias in Vaisala sensors noted by previous investigators [Soden *et al.*, 1994; Soden and Lanzante, 1996; Lesht, 1999; Lesht and Richardson, 2002; Turner and Goldsmith, 1999; Kley *et al.*, 2000; Guichard *et al.*, 2000; Wang *et al.*, 2002; Turner *et al.*, 2003].

[31] Table 2 provides a statistical summary of the number of observations, bias, RMS difference, and correlation between the radiosonde and GOES $T_{6.7}$. It is interesting to note that the dry bias in Vaisala radiosondes tends to be larger in the more recent IOPs (1999, 2000) relative to the earlier ones even though the contamination-induced bias in the Vaisala sensor (section 2.1) should have been smaller for the 1999 and 2000 IOPs (because of the younger age of the

radiosondes and thus less exposure to the contaminating packaging material). Despite these changes the bias in $T_{6.7}$ increased from ~ 3 K ($\sim 30\%$ relative bias in UTH) during the 1996 and 1997 IOPs to 4.5–5 K (~ 45 – 50% relative bias in UTH) during the 1999 and 2000 IOPs. This suggests that contamination by the packaging material may not be the primary cause of dry bias in the Vaisala sensors, that the corrections developed by Vaisala are ineffective, or that there is large batch-to-batch variability in the dry bias [Turner *et al.*, 2003].

[32] In addition to the RS80-H humidity sensors, a number of Vaisala RS90 sensors were also flown during the 2000 IOP. The $T_{6.7}$ calculations from the RS90 sensors are also shown in Figure 2 and Table 2. Despite the improvements in sensor design, the RS90 radiosondes also exhibit a distinct dry bias relative to GOES that is comparable in magnitude to that found in the RS80-H. The similarity between the RS80-H and RS90 sensors is further illustrated in Figure 3, which compares the time-average relative humidity from 34 dual-radiosonde launches in which both the RS80-H and RS90 sensors were carried on the same balloon. Both the RS80-H and RS90 profiles are uncorrected. Note that because of a change in sensor packaging, the RS90s will still have a time lag error (i.e., section 2.1.3), but should have considerably less contamination error than the RS80-H sensor. The RS90s profiles are slightly moister below ~ 500 hPa. However, above this level the RS80-H and RS90 profiles are virtually indistinguishable, except for the RS90 being slightly moister near 400 hPa and slightly drier near 200 hPa. The similarity between RS80-H and RS90 profiles is consistent with the presence of a large dry bias relative to GOES for both sensors (Figure 2).

[33] Figure 4 depicts histograms of UTH computed from the radiosonde measurements and from the corresponding subset of colocated GOES observations. Statistics for each distribution are listed in the upper right-hand corner. Both the GOES and radiosonde display a highly skewed distribution of UTH with a peak at the dry end and an elongated tail toward the moist end. The dry bias in radiosonde UTH is clearly manifest in the PDF as a shift toward drier conditions with the differences being most noticeable for $UTH < 10\%$.

[34] To more clearly illustrate the dependence of the radiosonde dry bias on the prevailing humidity conditions, Figure 5 displays a histogram of the fractional difference in UTH, (GOES-radiosonde)/GOES, binned as a function of the corresponding GOES UTH. The fractional bias in the radiosonde measurements is largest (~ 0.5) for the driest conditions ($UTH < 10\%$) and then decreases to less than half of that value (~ 0.25) as the UTH approaches $\sim 50\%$. This result suggests that the dry bias in the Vaisala sensor is strongly dependent upon the ambient humidity conditions, being larger for lower values of relative humidity. Attempts to correct for this bias should therefore include a mechanism to account for such dependence. Beyond 70% UTH, the fractional bias again increases to values in excess of 0.3; however, the number of observations in these bins is very small (Figure 3) and thus some caution is warranted when interpreting their significance. It is also possible that the increase in bias as one approaches the moist end of the distribution reflects a greater probability of cloud contam-

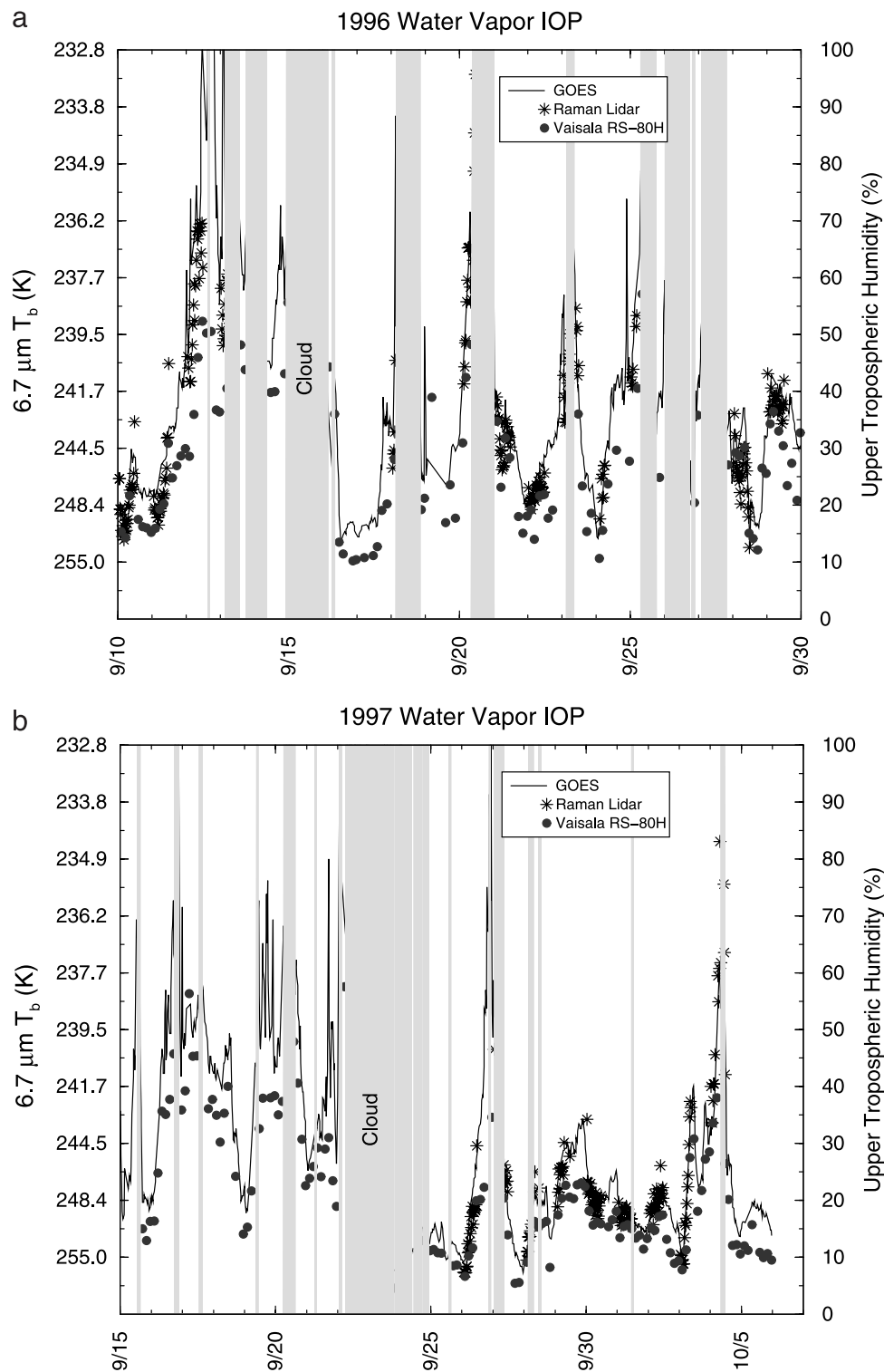


Figure 2. A comparison of the time series of GOES-observed $T_{6.7}$ (solid line) with that computed from radiative transfer calculations using the Raman lidar (stars) and unadjusted Vaisala RS80-H (solid circles) humidity profiles as input. Results are presented for (a) the 1996 IOP, (b) the 1997 IOP, (c) the 1999 IOP, and (d) the 2000 IOP. The 2000 IOP also contains radiosonde-simulated $T_{6.7}$ obtained using the Vaisala RS90 humidity sensor (open circles). Shaded regions indicate times when the GOES $T_{6.7}$ was believed to be contaminated by high-level cloud cover. The corresponding UTH scale is displayed on the right-hand side of each plot.

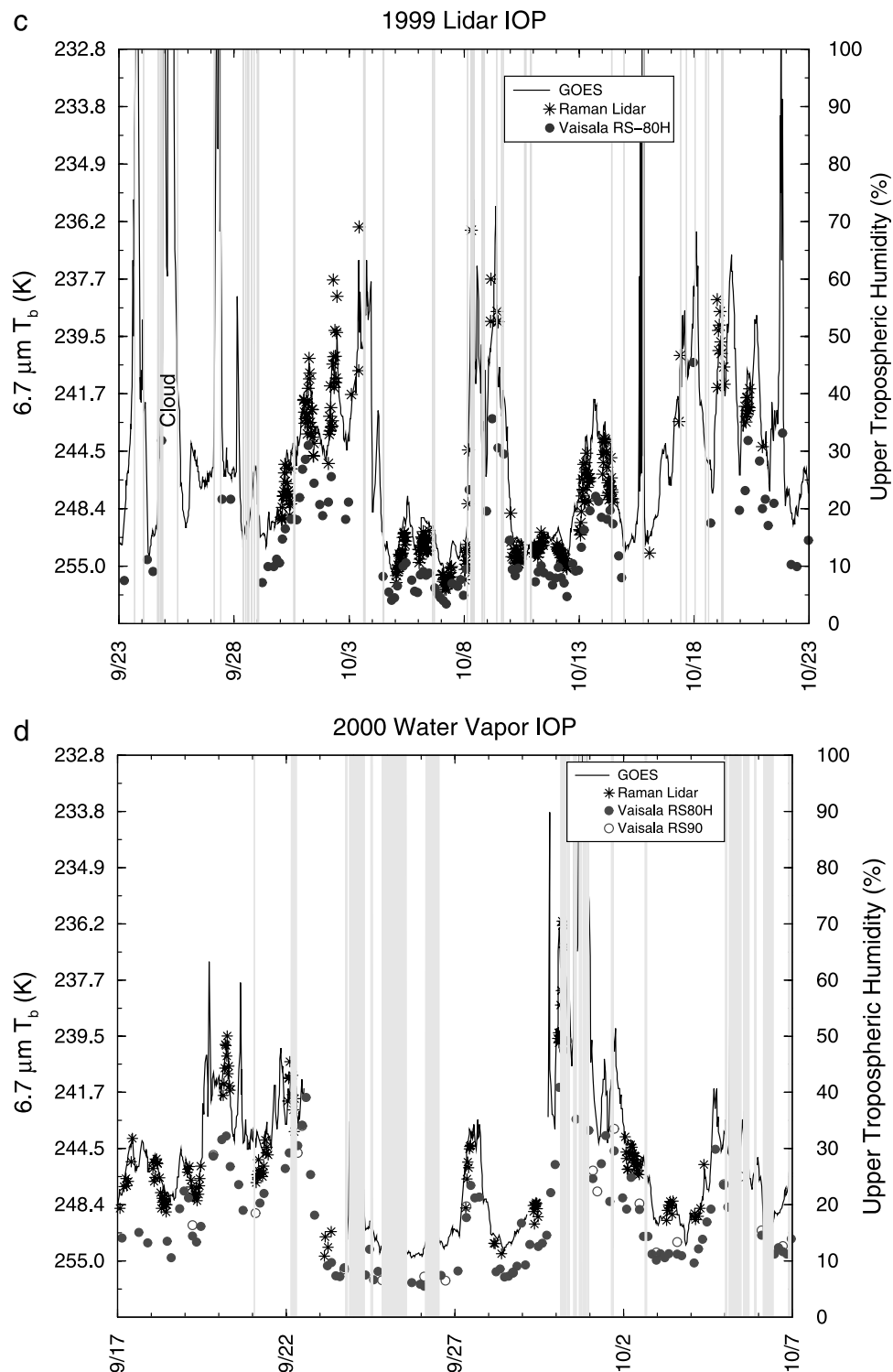


Figure 2. (continued)

ination in the GOES pixel (which would introduce a moist bias in the GOES measurement) as the UTH increases.

3.2. Lidar Versus GOES

[35] The time series of Raman lidar $T_{6.7}$ is also shown in Figure 2 for all four IOPs. Recall that the Raman lidar retrievals of UTH are only available during night. In

contrast to the radiosonde measurements, which are systematically drier than GOES, the lidar observations exhibit much better agreement with the GOES-observed $T_{6.7}$. The bias between GOES-observed and lidar-simulated $T_{6.7}$ (Table 3) ranges from ~ 0.5 K to 1.2 K. The average bias from all four IOPs is 1.1 K which corresponds to a relative error in UTH of $\sim 10\%$, indicating that the systematic

Table 2. Statistics of the Comparison Between Uncorrected Radiosonde-Simulated Radiances and Colocated GOES 8 Observed Radiances for Each IOP^a

IOP	N	Mean $T_{6.7}$	Bias	RMS	Correlation
1996	106	241.6	2.9	3.5	0.90
1997	123	244.2	3.0	3.3	0.96
1999	102	245.9	5.5	5.8	0.96
2000	100	244.2	4.7	5.0	0.94
2000 (RS90)	21	243.9	3.9	4.1	0.94

^aStatistics presented include the number of colocated GOES/radiosonde observations (N), the mean GOES $T_{6.7}$ (K) averaged over all colocated observations, the bias (K) in radiosonde $T_{6.7}$ relative to GOES, the RMS difference (K) between colocated GOES and radiosonde $T_{6.7}$, and the Pearson correlation coefficient between the GOES and radiosonde $T_{6.7}$. All results are for the Vaisala RS80-H sensors, except for the 2000 IOP, for which separate entries are provided for the RS80-H and RS90 sensors.

differences between the GOES and lidar measurements are within their estimated observational uncertainty (section 2). This level of consistency further supports the conclusion that the discrepancy between the GOES and radiosonde measurements is primarily attributable to a dry bias in the Vaisala sensor rather than to a cold bias in the GOES radiances.

[36] Note, however, that the lidar $T_{6.7}$ are also slightly warmer (drier) than GOES, suggesting that there may be a modest cold bias in either the GOES calibration or in the radiative transfer model used to compute the 6.7 μm radiance from the atmospheric profiles. Recent results from the ARM Fire Water Vapor Experiment (AFWEX) in which GOES 8 radiances were validated against spectrally resolved radiance measurements from the NASA Airborne Spectroradiometer Testbed-Interferometer (NAST-I) reveal excellent agreement between the two radiance measurements (bias < 0.25 K; Soden *et al.* [2002]), suggesting that any calibration error in GOES 8 is unlikely to be large enough to explain the ~ 1 K bias between GOES-observed and lidar-simulated radiances.

[37] Histograms of UTH computed from the lidar measurements also show better agreement with those derived from GOES (Figure 4). Both the GOES and lidar display very similar distributions, particularly at the dry end of the spectrum. Moreover, the distribution of bias between GOES and lidar UTH (Figure 5) exhibits little dependence on the prevailing humidity conditions. In contrast to the radiosonde bias which increased as the upper troposphere became drier, the fractional bias in the lidar measurements is relatively flat, varying from ~ 0.05 to 0.09 for $\text{UTH} < 70\%$.

[38] Above 70% UTH the fractional bias increases systematically such that the lidar becomes ~ 0.1 to ~ 0.4 times drier than GOES. The tendency for the dry bias in both the radiosonde and lidar to increase rapidly at high values of UTH further supports the hypothesis that the moist end of GOES radiance distribution may still contain some partial cloud contamination even after the cloud screening mask is applied. We note, however, that this feature remains even if the brightness temperature threshold for cloud screening is increased from 25 to 30 K, implying that the simple IR threshold approach used here may be inadequate to detect very thin clouds such as sub-visible cirrus. In principal, one could use the Raman lidar measurements to better detect the occurrence sub-visible cirrus clouds over the CART site. However, we elected not to use this method because of concerns regarding the differences in scale between the lidar and GOES pixel footprints which could lead contamination

of the GOES pixel in situations where thin cirrus cover a portion of the GOES pixel not observed by the lidar. Nevertheless, the Raman lidar does provide a powerful tool for assessing cloud-screening methods, particularly for thin cirrus, and should be considered in future investigations.

4. Impact of Radiosonde Corrections

[39] In this section, we examine the impact of existing correction procedures on the dry bias in the radiosonde humidity profiles. Three different procedures are considered: (1) a scheme developed by Vaisala that includes corrections for calibration, temperature, and contamination errors (described in section 2.1.1 and hereafter denoted as VS); (2) a correction based scaling the radiosonde water vapor profile so that the total column water vapor agrees with that retrieved from the MWR (described in section 2.1.2 and hereafter denoted as MS); and (3) a scheme that combines the Vaisala correction with a correction that accounts for a known time lag error in the Vaisala radiosondes caused by an exponential increase in the sensor's time constant with decreasing temperature (described in section 2.1.3 and hereafter denoted as LS).

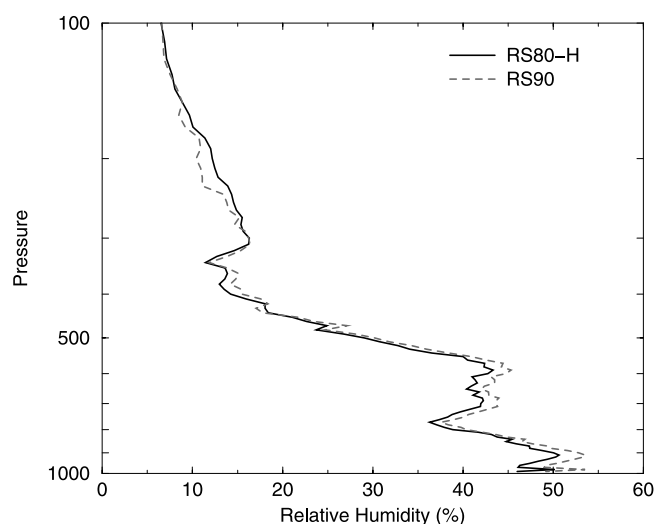


Figure 3. Time-average relative humidity (with respect to water) from 34 dual-launch radiosondes that carried both RS80-H (solid line) and RS90 (dashed line) sensors during the 2000 water vapor IOP. Both the RS80-H and RS90 profiles are uncorrected.

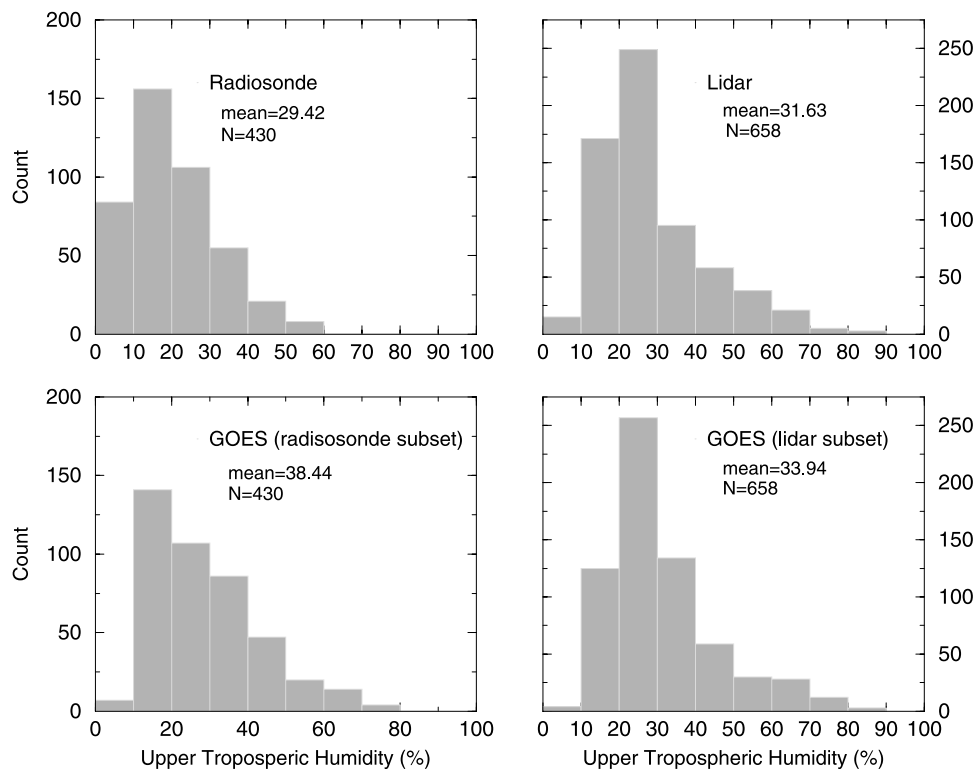


Figure 4. Composite histograms from all four IOPs of upper tropospheric relative humidity (UTH) for Vaisala RS80-H radiosonde observations (upper left), the subset of GOES observations that coincide with a radiosonde observation (lower left), Raman lidar observations (upper right), and the subset of GOES observations that coincide with a Raman lidar observation (lower right).

[40] For each correction procedure, the $T_{6.7}$ is recomputed using the adjusted moisture profiles and compared to the corresponding GOES-observed radiances. The results of this comparison are summarized in Tables 4–6 for the VS, MS, and LS corrections, respectively. For all four IOPs, the application of any one of the three correction schemes does reduce the discrepancy between the radiosonde-simulated and GOES-observed $T_{6.7}$. The reduction in the warm (dry) bias in radiosonde $T_{6.7}$ varies from ~ 0.5 K to as much as 1.5 K, depending upon both the type of correction

applied as well as the IOP under consideration. In general, the correction tends to be largest for those IOPs where the bias in the unadjusted radiosonde profiles is also largest. This suggests that the inter-IOP differences in the GOES-radiosonde biases are real and related to differences in UTH conditions between IOPs.

[41] Because the MWR retrievals are not always available (because of instrument down time or periods of heavy precipitation) all 3 corrections are not performed for every sounding and the number of observations differs depending

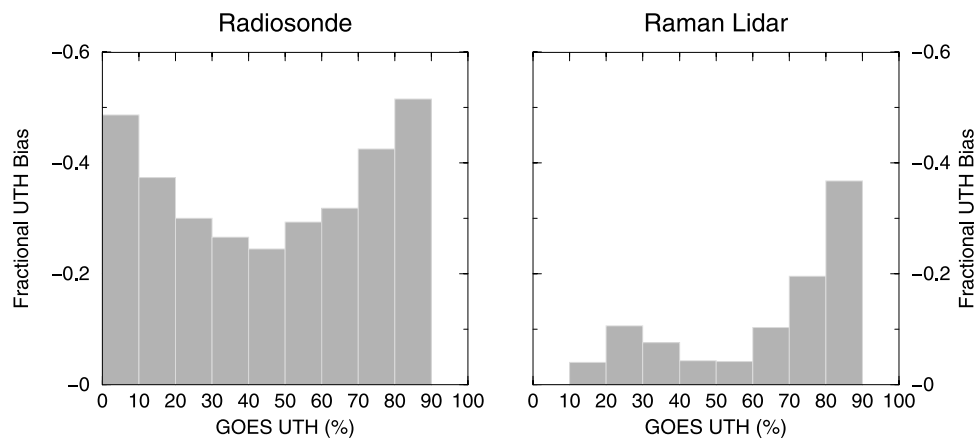


Figure 5. Fractional UTH bias relative to GOES plotted as a function of UTH for the Vaisala RS80-H radiosonde observations (left) and Raman lidar observations (right). The results are averages from all four IOPs.

Table 3. Statistics of the Comparison Between Lidar-Simulated Radiances and Colocated GOES 8 Observed Radiances for Each IOP^a

IOP	N	Mean $T_{6,7}$	Bias	RMS	Correlation
1996	239	242.1	1.2	2.1	0.91
1997	150	246.4	0.5	1.6	0.96
1999	300	247.2	1.5	2.1	0.98
2000	257	244.3	0.9	1.2	0.90

^aStatistics presented include the number of colocated GOES/lidar observations (N), the mean lidar $T_{6,7}$ (K) averaged over all colocated observations, the bias (K) in lidar $T_{6,7}$ relative to GOES, the RMS difference (K) between colocated GOES and lidar $T_{6,7}$, and the Pearson correlation coefficient between the GOES and lidar $T_{6,7}$.

upon which correction procedure is being considered. To eliminate this difference in sampling and enable a more accurate assessment of the relative effectiveness of the 3 correction procedures, Figure 6 compares the bias in $T_{6,7}$ for each IOP using only those soundings for which all 3 corrections are available. The MS correction, which uses the observed MWR precipitable water to scale the radiosonde profile, is generally the least successful of the three procedures for reducing the dry bias relative to GOES. For example, during the 1999 IOP the MS correction is only about one-third the magnitude of the LS and VS corrections. Since the MS correction scales the radiosonde total column water vapor to match that retrieved from the MWR, it is most effective in the lower troposphere where the bulk of the water vapor mass resides. However, because of the colder, drier conditions in the upper troposphere, the dry bias in the Vaisala sensors tends to increase with height [Elliott and Gaffen, 1991]. As a result the MS correction, which implicitly assumes a vertically uniform relative bias in the humidity sounding, will systematically underestimate the magnitude of the dry bias in the upper troposphere. In contrast, both the VS and LS procedures contain temperature- and relative-humidity-dependent corrections that can, in principal, account for a height-dependent bias.

[42] Of the three correction methods, the LS correction is generally the most effective at reducing the bias between the GOES-observed and radiosonde-simulated $T_{6,7}$. This reflects the fact that it contains both the Vaisala corrections (VS) as well as a time lag correction, which, on average, tends to moisten the upper troposphere. The LS correction typically reduces the bias by as much as 1–1.5 K, although a noticeably smaller reduction is obtained for the 1996 IOP. The VS correction, on the other hand, is typically around 0.6–0.7 K, with the exception of the 1999 IOP for which it is ~ 1.3 K. Although all of these correction procedures bring the GOES and radiosonde observations into better agreement, there still remains a sizable warm (dry) bias between the GOES-observed and radiosonde-simulated $T_{6,7}$, which

ranges from ~ 2.5 to 5 K (or roughly 0.25–0.5 in terms of the fractional bias in UTH).

5. Vertical Structure of the Humidity Profiles

[43] To examine the vertical structure of the radiosonde errors and the impact that the correction procedures have on that structure, Figure 7 compares the time-average relative humidity profiles from both the original and corrected radiosonde soundings to that retrieved from the Raman lidar. The mean profiles are shown separately for each IOP and the humidities are expressed relative to water. To eliminate sampling differences, time averages are computed from only those soundings where all 3 radiosonde correction procedures and the Raman lidar retrieval are available.

[44] In all four IOPs, the radiosonde and Raman lidar profiles of humidity exhibit excellent agreement below ~ 500 hPa. However, above this level the lidar soundings are systematically wetter than that measured by the radiosondes with the largest bias occurring between 200–400 hPa where the lidar relative humidity is nearly twice as large as that measured by the radiosonde. Note, however, that the shapes of the radiosonde and lidar humidity profiles do share some general similarities. Both show maxima near the surface decreasing to local minima around 500 hPa, and often containing a weak secondary maximum near ~ 700 hPa. Above 500 hPa, another local maximum (typically around 300 hPa) is found, although its presence is much more pronounced in the Raman lidar retrievals. Above this level, the Raman lidar retrievals decrease to a minima near 200 hPa and then tend to increase rapidly as one approaches the tropopause. This increase in humidity toward the tropopause is consistent with the formation of thin, nonconvective cirrus near the tropopause, which has been argued to result from slow rising motion below the tropopause associated with a region of net radiative heating [Jensen *et al.*, 2001]. The radiosondes, in contrast, decrease monotonically above 300 hPa. Of the three corrections, the LS correction tends

Table 4. As in Table 2, Except That This Table Compares the Vaisala-Adjusted Radiosonde Observations (VS Correction) Versus GOES 8

IOP	N	Mean $T_{6,7}$	Bias	RMS	Correlation
1996	106	241.6	2.3	3.1	0.87
1997	123	244.2	2.3	2.7	0.96
1999	102	245.9	4.2	4.6	0.97
2000	68	244.1	4.0	4.4	0.93

Table 5. As in Table 2, Except That This Table Compares the MWR-Adjusted Radiosonde Observations (MS Correction) Versus GOES 8

IOP	N	Mean $T_{6.7}$	Bias	RMS	Correlation
1996	46	242.1	2.7	3.2	0.92
1997	95	243.9	2.6	3.0	0.97
1999	96	246.1	5.2	5.5	0.97
2000	77	243.5	3.7	4.1	0.95

to provide the largest increases in upper level humidity. This is most evident for the 1996 IOP, where it adds as much as 10% more relative humidity between 200 and 400 hPa.

[45] Because the Raman lidar retrievals require only a single calibration for the entire humidity profile, the vertical structure of the lidar humidity profile is a robust feature of the retrieval [Turner and Goldsmith, 1999]. One potential source of error in the lidar retrieval is that the Raman scattering cross-section for the water vapor molecule does contain a temperature dependence that is not accounted for in these retrievals and that can introduce a height-dependent bias in the retrieved humidity profile [Whiteman, 2003a]. However, recent estimates [Ferrare et al., 2002; Whiteman, 2003b] suggest that this will introduce no more than a 0.04 fractional error in the upper tropospheric humidity profile and thus would only account for a very small portion (~10%) of the discrepancy shown in Figure 7. Thus discrepancies in the vertical structure of the humidity profile between radiosonde and lidar measurements are unlikely to stem from a height-dependent bias in the Raman lidar retrieval, and the good agreement between the lidar and radiosonde in the lower troposphere further suggests that the upper tropospheric discrepancy is attributable to a dry bias in the radiosonde soundings.

[46] To better illustrate the nature of the differences in the vertical structure of relative humidity, Figure 8 compares a case study of the time series of relative humidity profiles for the period of 17–22 September 2000 from the Raman lidar (Figure 8c) and uncorrected radiosondes (Figure 8b). For reference, Figure 8a depicts the corresponding time series of $T_{6.7}$ (and UTH) taken from Figure 2. To illustrate the impact of the radiosonde corrections, the $T_{6.7}$ are presented for both the uncorrected and corrected radiosonde profiles. While both the radiosonde and lidar depict a similar evolution of water vapor below 500 mb, the Raman lidar clearly shows a sequence of much larger upper tropospheric humidity values between 19–22 September. During this period the Raman lidar frequently records relative humidities in excess of 60%, whereas the radiosondes are typically measuring values of around 30% (i.e., a fractional dry bias of ~0.5). This corresponds to the same periods when the radiosonde $T_{6.7}$ was significantly warmer (drier) than GOES. While the

corrections generally move the radiosonde $T_{6.7}$ toward the GOES-observed values, none of them are able to achieve the level of agreement found between the GOES and Raman lidar measurements.

6. Radiance Assimilation

[47] As demonstrated in the preceding section, even the most effective of the existing correction procedures is unable to significantly reduce the upper tropospheric dry bias in the radiosonde measurements compared to either the GOES or Raman lidar. In this section, we outline an alternative strategy for adjusting the radiosonde humidity profiles based on a one-dimensional variational assimilation of the GOES 6.7 μm radiances. The assimilation procedure outlined below modifies the original radiosonde humidity profile to yield a radiance-adjusted humidity profile that is consistent with both the GOES-observed $T_{6.7}$ and assumptions regarding the error characteristics of the GOES and radiosonde data. The effectiveness of this approach is then evaluated by comparing the resulting radiance-adjusted humidity profile against coincident Raman lidar observations.

[48] From a variational perspective, the radiance assimilation may be expressed as [Daley, 1991]

$$\mathbf{r}^a = \mathbf{r} + \mathbf{B}\mathbf{H}^T(\mathbf{H}\mathbf{B}\mathbf{H}^T + \mathbf{C})^{-1}(\mathbf{y} - h(\mathbf{r})), \quad (7)$$

where \mathbf{r} represents the original radiosonde humidity profile, \mathbf{r}^a is the resulting radiance-adjusted humidity profile, \mathbf{y} is the GOES-observed $T_{6.7}$, and \mathbf{B} and \mathbf{C} represent the error covariance matrices for the radiosonde humidity profile and GOES observations respectively. A key component of any radiance assimilation is the forward operator h which transforms the original radiosonde humidity profile \mathbf{r} into its equivalent radiance units (i.e., into a 6.7 μm brightness temperature) and the Jacobian \mathbf{H} which defines the differential behavior of the radiance quantity with respect to the state variable under consideration; i.e., $\mathbf{H} \equiv \partial h(\mathbf{r})/\partial \mathbf{r}$. In conventional radiance assimilation methods h is computed using a full radiative transfer model and, consequently, \mathbf{H} is typically a nonlinear function that requires iteration to obtain

Table 6. As in Table 2, Except That This Table Compares the Time-Lag-Adjusted Radiosonde Observations (LS Correction) Versus GOES 8

IOP	N	Mean $T_{6.7}$	Bias	RMS	Correlation
1996	106	241.6	2.2	3.5	0.89
1997	122	244.2	2.1	2.5	0.96
1999	102	245.9	4.1	4.4	0.97
2000	86	244.2	3.3	3.7	0.94

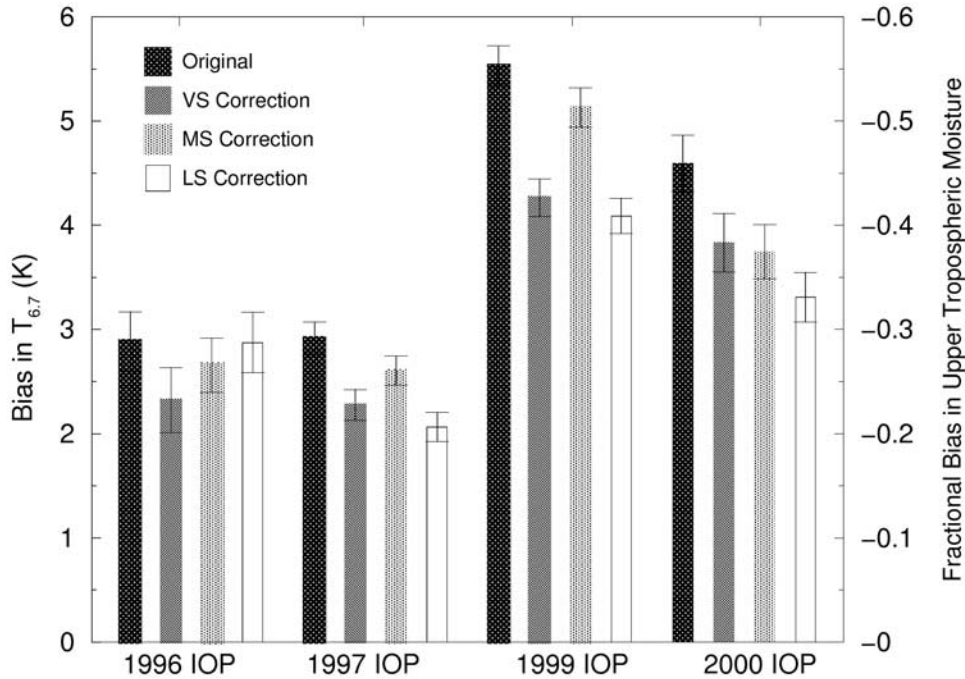


Figure 6. Bias in $T_{6.7}$ relative to GOES (i.e., radiosonde - GOES) for the original (uncorrected), the VS-corrected, the MS-corrected, and the LS-corrected radiosonde profiles. Results are displayed separately for each IOP. The vertical bars depict the standard error of the bias. The scale on the right-hand side displays the corresponding fractional bias in upper tropospheric water vapor. Note that the sign of the UTH scale is the opposite of that for $T_{6.7}$; that is, a warm bias in $T_{6.7}$ corresponds to a dry bias in UTH.

an optimal solution. Here we introduce an analytical formula for computing \mathbf{H} that provides a linear relationship between $T_{6.7}$ and the natural logarithm of the vertically weighted relative humidity field. The advantage of this approach over the use of explicit radiative transfer calculations is that it enables equation (7) to be reduced to a simple analytical expression that requires no iteration. The analytical formula also provides a straightforward interpretation of the radiance assimilation process in terms of a physically based scaling of the original humidity profile. As shown below, it is also highly effective in reducing the dry bias in the radiosonde humidity measurements.

[49] From equation (5) we express $h(\mathbf{r})$ in terms of the weighted average of the humidity profile

$$h(\mathbf{r}) = \left[\ln \left(\sum_i w_i r_i \right) p_0 / \cos \theta - a \right] / b, \quad (8)$$

where w_i and r_i represent the channel weighting function and relative humidity at each level i in the profile, and $\cos \theta$, p_0 , a , and b are as in equation (5). We use the standard pressure level weights for the $6.7 \mu\text{m}$ channel listed in Table 2 of Soden and Bretherton [1993]. Neglecting variations in p_0 , the Jacobian of equation (8) is

$$H_i \equiv \frac{\partial h(\mathbf{r})}{\partial r_i} = \frac{w_i}{b \hat{r}}, \quad (9)$$

where $\hat{r} \equiv \mathbf{w} \bullet \mathbf{r}$. We approximate $\mathbf{B} = \sigma^2 \mathbf{I}$, where \mathbf{I} is the identity matrix and σ^2 is the error variance in

the radiosonde humidity profile which is assumed to be independent of height. By neglecting the off-diagonal terms in \mathbf{B} , we implicitly assume that the vertical decorrelation scale of radiosonde humidity errors is much smaller than the decorrelation scale of the $6.7 \mu\text{m}$ weighting function. This assumption is justified given the relatively large depth of the weighting function (Figure 1) and the lack of independent information regarding the vertical error structure in the radiosonde humidity measurements. As shown in Figure 1, the typical weighting function has a depth of several kilometers, thus our neglect of vertical decorrelation errors in the radiosonde profile assumes that the radiosonde humidity errors decorrelate at depth scales of a few kilometers or less. The insensitivity of the assimilation procedure to error correlations at smaller scales reflects the fundamental lack of information content in the $6.7 \mu\text{m}$ channel to humidity fluctuations at finer vertical resolutions [Soden and Bretherton, 1993]. The $6.7 \mu\text{m}$ channel does not provide information on the vertical structure of the upper tropospheric humidity profile, but rather is sensitive to a deep-layer mean centered in the upper troposphere. In principle, one could derive empirical functions to describe the vertical humidity error correlations based upon the lidar/radiosonde comparisons. However, this would leave us with no independent set of observations to verify the impact of the radiance assimilation. That is, the radiance-adjusted humidity profiles would agree with the Raman lidar profiles (at least in part) because we have already used the lidar data to define the error correlations. Instead, we have chosen to keep the radiance adjustment procedure

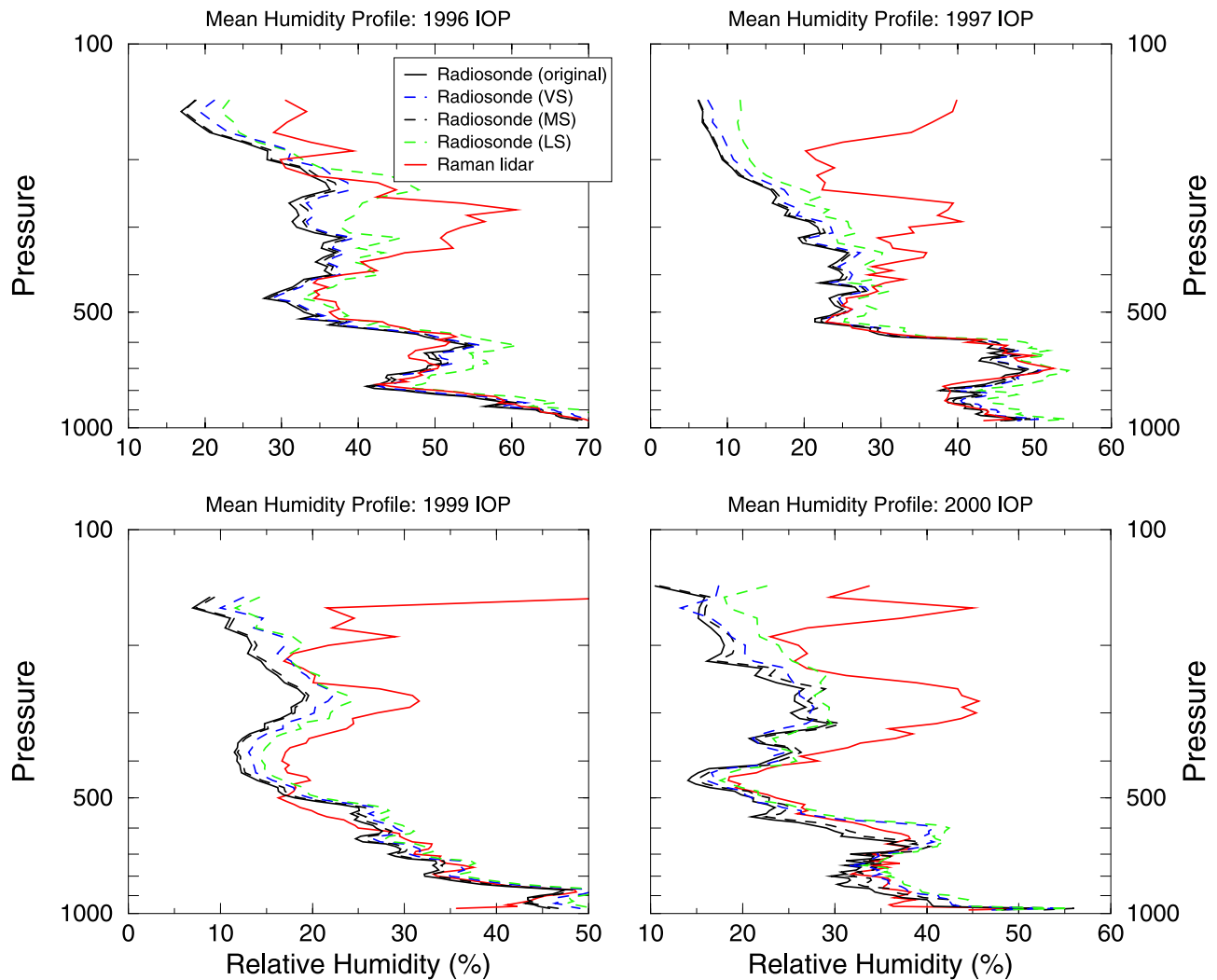


Figure 7. Time-average relative humidity profiles (with respect to water) from both the original and corrected radiosonde soundings compared to the Raman lidar retrievals for the 1996 IOP (upper left), 1997 IOP (upper right), 1999 IOP (lower left), and 2000 IOP (lower right). To eliminate sampling differences, time averages are computed from only those soundings where all three radiosonde correction procedures and the Raman lidar retrieval are available.

free of any information from the lidar, and can therefore use the lidar data as an independent verification of the procedure's effectiveness.

[50] Because the error variance in the radiosonde humidity profiles (relative to the Raman lidar) is roughly an order of magnitude larger than that for GOES, we further simplify (7) by assuming that $C \ll \mathbf{HBH}^T$; that is, the total error variance is dominated by the error variance in the radiosonde profile. The result is a simple analytical formula for scaling the radiosonde humidity profile, based upon the difference in brightness temperature between the GOES and radiosonde $\Delta T_{6,7}$:

$$r_i^a = r_i(1 + \Gamma_i b \Delta T_{6,7}). \quad (10)$$

As in equation (5), b represents the fractional change in the humidity profile per degree difference in brightness temperature between the radiosonde and GOES ($\Delta T_{6,7}$) and Γ_i defines the contribution each level i makes to the

vertically integrated response of the channel weighting function and is given by

$$\Gamma_i = \frac{\hat{r}}{r_i} \frac{w_i}{\sum_j w_j^2}. \quad (11)$$

For applications in which the error variance in the satellite radiance is not negligible, it can be accounted for simply by scaling Γ_i by a factor of $1/(1 + \gamma)$, where γ represents the ratio of the corresponding error variance in the satellite measurements to that for the radiosonde. Estimate of the uncertainty in GOES 8 calibration of the $T_{6,7}$ are roughly 0.5–1 K [Soden *et al.*, 2002] with a corresponding noise-equivalent delta-temperature of 0.2 K. From equation (6), this corresponds to uncertainties in relative humidity of approximately 5–10% and 2% respectively.

[51] Figure 9 compares the time-average relative humidity profiles from both the original and radiance-adjusted

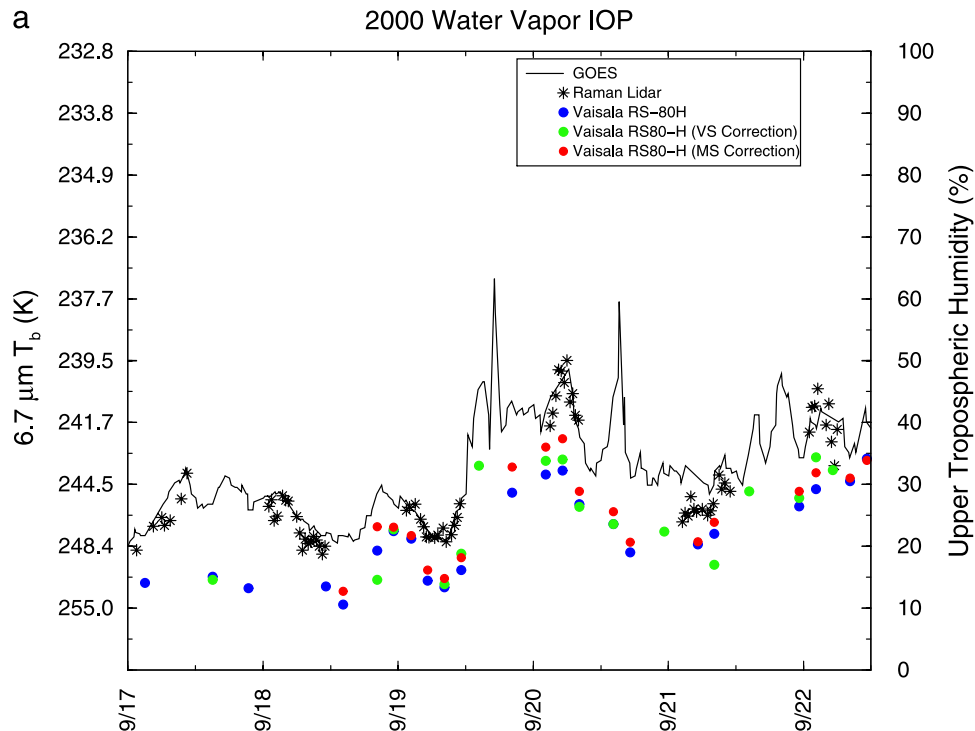


Figure 8. (a) Time series of the $T_{6.7}$ and UTH and (b and c) corresponding profiles of relative humidity for 17–22 September 2000. The time series of $T_{6.7}$ and UTH are shown for the GOES, Raman lidar, and both corrected and uncorrected radiosondes (Figure 8a). Figures 8b and 8c display profiles from uncorrected radiosondes and the Raman lidar, respectively.

soundings to that retrieved from the Raman lidar. The mean profiles are shown separately for each IOP and, as in Figure 7, the humidities are expressed relative to water. To eliminate sampling differences, time averages are computed from only those soundings where both the Raman lidar and GOES radiances were available within ± 30 min of the radiosonde launch.

[52] Below 500 hPa the radiance assimilation has virtually no impact on the humidity profiles because the GOES weighting function receives little contribution from these levels (e.g., Figure 1). However, for the levels between 200–500 hPa, the radiance assimilation significantly improves the humidity profile as compared to the Raman lidar observations. In all four IOPs, the assimilation of GOES radiances is far more effective than any of the existing radiosonde correction procedures at reducing the dry bias relative to the Raman lidar. For the 1996, 1997 and 1999 IOPs, the radiance assimilation reduces the fractional dry bias between 200 and 500 hPa from ~ 0.4 to less than 0.1. In comparison, the dry bias from the adjusted radiosonde profiles in Figure 7 range from ~ 0.3 to 0.4. For the 2000 IOP the impact of radiance assimilation is not as large as obtained for the other IOPs, but it still outperforms any of the existing corrections in terms of the agreement with Raman lidar profiles.

[53] Above 200 hPa, the radiance assimilation provides little change from the original radiosonde humidity profile, again because of the lack of a significant contribution from the $6.7 \mu\text{m}$ weighting function at these levels. In particular, the radiance-adjusted profiles are unable to capture the trend

toward increased relative humidity above ~ 150 hPa observed by the Raman lidar. This reflects an inherent limitation of the $6.7 \mu\text{m}$ channel. In addition to its lack of significant contribution from these levels, the weighting function also lacks the vertical resolution necessary to resolve such variability [Engelen and Stephens, 1999].

7. Conclusions

[54] Observations of upper tropospheric humidity from the $6.7 \mu\text{m}$ channel of GOES 8 were compared with Raman lidar and Vaisala radiosonde measurements obtained during four different ARM IOPs at the SGP/CART facility in central Oklahoma. During all four IOPs, excellent agreement was observed between the GOES and Raman lidar observations of upper tropospheric humidity. Systematic differences in $T_{6.7}$ ranged from 0.5 to 0.12 K, or roughly 5–10% in terms of the UTH. The good agreement between GOES and Raman lidar observations encourages the use of both instruments for describing the spatial and temporal variability of upper tropospheric water vapor. The fact that GOES provides excellent horizontal coverage but lacks information on the vertical structure, while the Raman lidar provides excellent information on the vertical structure but lacks information on the horizontal distribution illustrates the complimentary nature of the two observing systems. Future work will investigate the potential for combining these measurements to generate a full three-dimensional description of the water vapor distribution over the SGP/CART site.

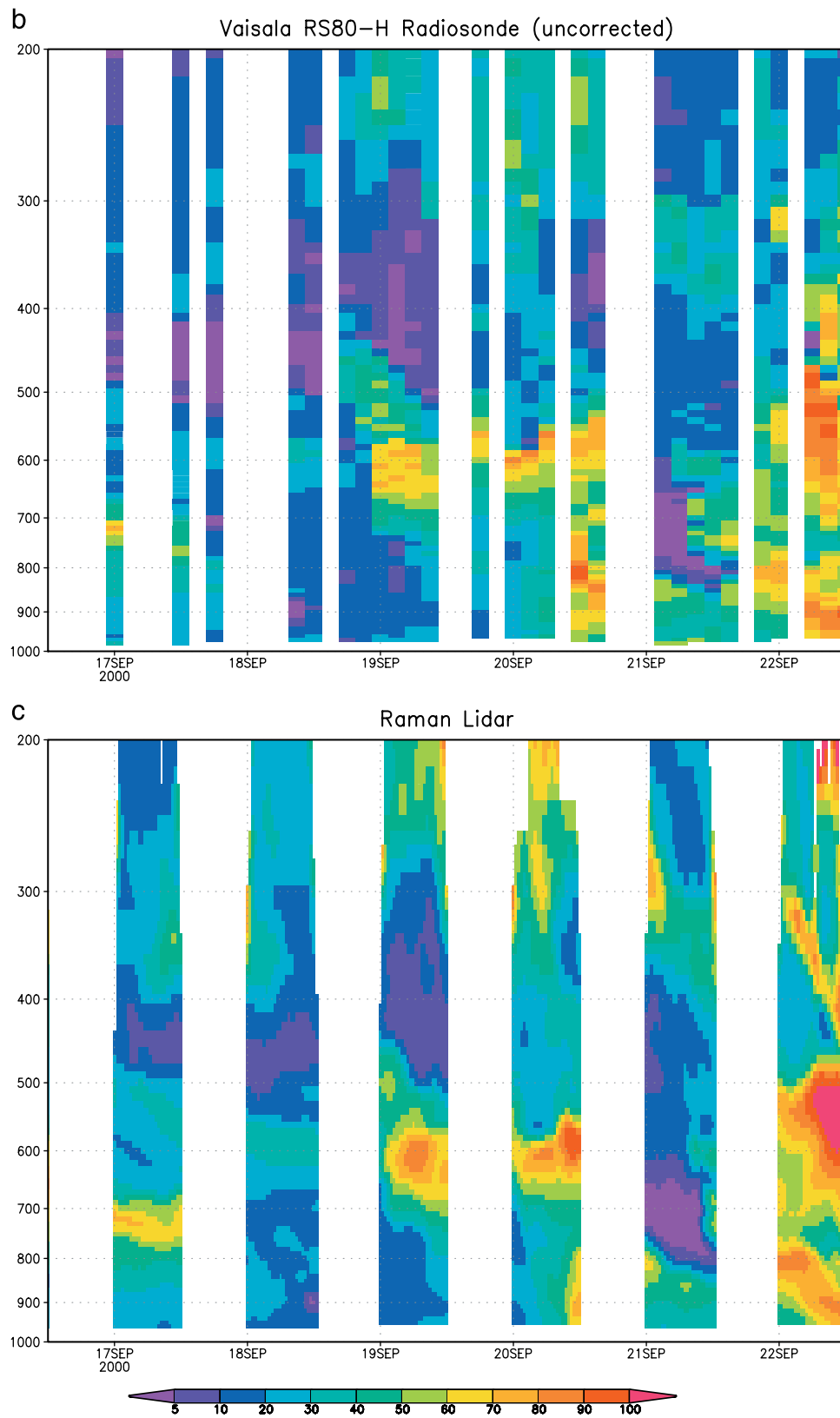


Figure 8. (continued)

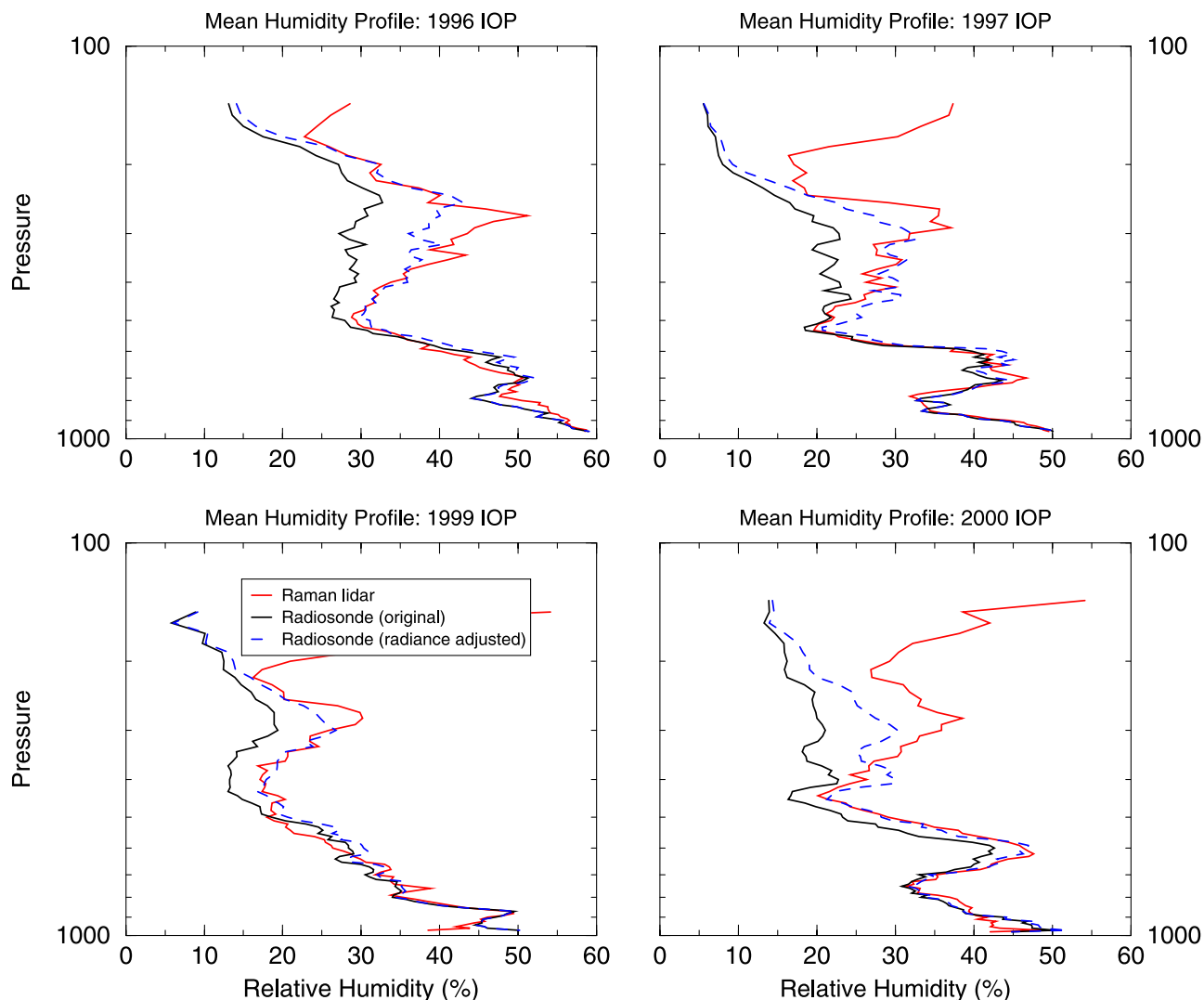


Figure 9. Time-average relative humidity profiles (with respect to water) from both the original and radiance-adjusted radiosonde soundings compared to the Raman lidar retrievals for the 1996 IOP (upper left), 1997 IOP (upper right), 1999 IOP (lower left), and 2000 IOP (lower right). To eliminate sampling differences, time averages are computed from only those soundings where the radiosonde, GOES, and Raman lidar observations are all available.

[55] In contrast, radiosondes equipped with Vaisala RS80-H and RS90 sensors were found to be systematically drier in the upper troposphere by 30–40% relative to both the Raman lidar and GOES measurements. These results reinforce several previous intercomparison studies that have found the Vaisala sensors to exhibit a dry bias. Comparison with Raman lidar measurements indicates that this bias is most pronounced in the upper troposphere (above ~ 500 hPa) and appears to be unrelated to the age or vintage of the humidity sensor used. A histogram analysis of the difference between GOES and Vaisala UTH indicated that the largest (fractional) dry biases are observed at the lowest humidity values. The fact that the comparisons were restricted to cloud-free conditions may therefore introduce a sampling bias into the results, which emphasizes conditions in which the radiosondes have the greatest difficulty (i.e., clear, dry profiles).

[56] The impact of three different “correction” procedures designed to rectify known deficiencies in the radio-

sonde humidity sensors was examined. While useful for the lower troposphere, we found that these algorithms offered little improvement in the upper troposphere where the dry bias in Vaisala sensors was most pronounced. An alternative strategy, based on variational assimilation of satellite radiances, was outlined and, when applied to the radiosonde measurements, was found to significantly improve their agreement with coincident Raman lidar observations. In most instances, the radiance assimilation was able to reduce the fractional dry bias in upper tropospheric water vapor from ~ 0.4 to < 0.1 , which places it within the level of uncertainty in the forward radiance models and within the levels of discrepancy between the Raman lidar and GOES measurements.

[57] Several previous studies [Elliott and Gaffen, 1991; Soden and Lanzante, 1996; Ross and Gaffen, 1998; Free et al., 2002] have documented the presence of spatial and temporal discontinuities in the global radiosonde humidity records that largely stem from changes in instrumentation

and reporting practices. Such discontinuities greatly impede its use for climate studies and, as a result, our knowledge regarding the long-term changes in water vapor, particularly in the upper troposphere, is lacking. The success of the radiance assimilation method demonstrated above suggests that a similar strategy could be used to correct deficiencies in the global historical radiosonde record using intercalibrated, multispectral radiances from TOVS [Bates et al., 1996]. The global coverage and length of the TOVS archive (dating back to 1978) combined with the presence of multiple water vapor channels (centered at 6.7, 7.3 and 8.3 μm) offers the potential to create a climate-quality record from the global radiosonde humidity soundings over the past two and one-half decades.

[58] **Acknowledgments.** This work was conducted as part of the ARM program sponsored by the U.S. Department of Energy, Office of Energy Research, Office of Health and Environmental Research, Environmental Sciences Division.

References

- Bates, J. J., and D. L. Jackson (2001), Trends in upper tropospheric humidity, *Geophys. Res. Lett.*, **28**, 1695–1699.
- Bates, J. J., X. Wu, and D. L. Jackson (1996), Interannual variability of upper tropospheric water vapor brightness temperature, *J. Clim.*, **9**, 427–438.
- Chiou, E. W., M. P. McCormick, and W. P. Chu (1997), Global water vapor distributions in the upper troposphere and lower stratosphere from 5.5 years of SAGE II observations, *J. Geophys. Res.*, **102**, 19,105–19,118.
- Daley, R. (1991), *Atmospheric Data Analysis*, 457 pp., Cambridge Univ. Press, New York.
- Elliott, W. P., and D. J. Gaffen (1991), On the utility of radiosonde humidity archives for climate studies, *Bull. Am. Meteorol. Soc.*, **72**, 1507–1520.
- Engelen, R. J., and G. L. Stephens (1998), Comparison between TOVS/HIRS and SSM/T-2 derived upper tropospheric humidity, *Bull. Am. Meteorol. Soc.*, **74**, 1323–1325.
- Engelen, R. J., and G. L. Stephens (1999), Characterization of water vapor retrievals from TOVS/HIRS and SSM/T-2 measurements, *Q. J. R. Meteorol. Soc.*, **125**, 331–351.
- Ferrare, R. A., S. H. Melfi, D. N. Whiteman, K. D. Evans, F. J. Schmidlin, and D. O' C. Starr (1995), A comparison of water vapor measurements made by Raman lidar and radiosondes Atmos, *J. Oceanic Technol.*, **12**, 1177–1195.
- Ferrare, R. A., et al. (2002), Raman lidar profiling of aerosols and water vapor over the Southern Great Plains, paper presented at Twelfth Atmospheric Radiation Measurement (ARM) Science Team Meeting, U.S. Dep. of Energy, St. Petersburg, Fla., 8–12 April.
- Free, M. P., et al. (2002), Creating climate reference datasets: CARDS workshop on adjusting radiosonde temperature data for climate monitoring, *Bull. Am. Meteorol. Soc.*, **83**, 891–899.
- Goldsmith, J. E. M., F. H. Blair, S. E. Bisson, and D. D. Turner (1998), Turn-key Raman lidar for profiling atmospheric water vapor, clouds, and aerosols, *Appl. Opt.*, **37**, 4979–4990.
- Goody, R. M. (1964), *Atmospheric Radiation*, vol. 1, *Theoretical Basis*, Oxford Univ. Press, New York.
- Guichard, F., D. Parsons, and E. Miller (2000), Thermodynamic and radiative impact of the correction of sounding humidity bias in the tropics, *J. Clim.*, **13**, 3611–3624.
- Held, I. M., and B. J. Soden (2000), Water vapor feedback and global warming, *Annu. Rev. Energy Environ.*, **25**, 441–475.
- Heymsfield, A. J., L. M. Miloshevich, G. Sachse, C. Twohy, and S. Oltmans (1998), Upper-tropospheric relative humidity observations and implications for cirrus ice nucleation, *Geophys. Res. Lett.*, **25**, 1343–1346.
- Jensen, E., L. Pfister, S. A. Ackerman, O. B. Toon, and A. Tabazedeh (2001), A conceptual model of dehydration of air due to freeze drying by optically-thin laminar cirrus rising slowly across the tropical tropopause, *J. Geophys. Res.*, **106**, 17,237–17,252.
- Kley, D., J. M. Russell III, and C. Phillips (Eds.) (2000), SPARC Assessment of upper tropospheric and stratospheric water vapour, *WMO/TD-143*, World Clim. Res. Programme, Geneva.
- Lesht, B. M. (1999), Reanalysis of radiosonde data from the 1996 and 1997 water vapor IOPs, paper presented at Ninth Atmospheric Radiation Measurement (ARM) Science Team Meeting, U.S. Dep. of Energy, San Antonio, Tex., 22–26 March.
- Lesht, B. M., and J. C. Liljegren (1997), Comparison of precipitable water vapor measurements obtained by microwave radiometers and radiosondes at the Southern Great Plains Cloud and Radiation Testbed Site, in *Proceedings of the Sixth Atmospheric Radiation Measurement (ARM) Science Team Meeting*, San Antonio, TX, pp. 165–168, U.S. Dep. of Energy, Washington, D. C.
- Lesht, B. M., and S. J. Richardson (2002), The Vaisala RS80-H dry bias correction redux, paper presented at Twelfth Atmospheric Radiation Measurement (ARM) Science Team Meeting, U.S. Dep. of Energy, St. Petersburg, Fla., 8–12 April.
- Liljegren, J. C. (2000), Automatic self-calibration of the ARM microwave radiometers, in *Microwave Radiometry and Remote Sensing of the Environment*, edited by P. Pampaloni, pp. 433–441, VSP Press, Utrecht, Netherlands.
- Menzel, W. P., F. Holt, T. J. Schmit, R. M. Aune, G. S. Wade, and D. G. Gray (1998), Application of GOES-8/9 soundings to weather forecasting and nowcasting, *Bull. Am. Meteorol. Soc.*, **79**, 2059–2078.
- Miloshevich, L. M., H. Vomel, A. Paukkunen, A. J. Heymsfield, and S. J. Oltmans (2001), Characterization and correction of relative humidity measurements from Vaisala RS80A radiosondes at cold temperatures, *J. Atmos. Oceanic Technol.*, **18**, 135–155.
- Miloshevich, L. M., H. Vomel, S. J. Oltmans, and A. Paukkunen (2003), In-situ validation of a correction for time-lag and bias errors in Vaisala RS80-H radiosonde humidity measurements, paper presented at 13th ARM Science Team Meeting, U.S. Dep. of Energy, Broomfield, Colo., 31 March to 4 April.
- Moody, J. L., A. J. Wimmers, and J. Davenport (1999), Remotely-sensed specific humidity: Development of a derived product from the GOES imager channel 3, *Geophys. Res. Lett.*, **26**, 59–62.
- Penney, G. M., and M. Lapp (1976), Raman-scattering cross-section for water vapor, *J. Opt. Soc. Am.*, **66**, 422–425.
- Revercomb, H. E., et al. (2003), The Atmospheric Radiation Measurement Program's water vapor intensive observation periods: Overview, initial accomplishments, and future challenges, *Bull. Am. Meteorol. Soc.*, **84**, 217–236.
- Richardson, S. J., M. E. Splitt, and B. M. Lesht (2000), Enhancement of ARM surface meteorological observations during the fall 1996 water vapor IOP, *J. Atmos. Oceanic Technol.*, **17**, 312–322.
- Ross, R. J., and D. J. Gaffen (1998), Comment on "Widespread tropical atmospheric drying from 1979 to 1995," *Geophys. Res. Lett.*, **25**, 4357–4358.
- Schmetz, J., and O. M. Turpeinen (1988), Estimation of the upper tropospheric relative humidity field from Meteosat water vapor image data, *J. Clim. Appl. Meteorol.*, **27**, 889–899.
- Schmetz, J., W. P. Menzel, C. Velden, X. Wu, L. van de Berg, S. Nieman, C. Hayden, K. Holmund, and C. Gejo (1995), Monthly mean large-scale analyses of upper tropospheric humidity and wind fields derived from three geostationary satellites, *Bull. Am. Meteorol. Soc.*, **76**, 1578–1584.
- Slingo, A. J., and M. J. Webb (1997), The spectral signature of global warming, *Q. J. R. Meteorol. Soc.*, **123**, 293–307.
- Soden, B. J. (1998), Tracking upper tropospheric water vapor: A satellite perspective, *J. Geophys. Res.*, **103**, 17,069–17,081.
- Soden, B. J., and F. P. Bretherton (1993), Upper tropospheric relative humidity from the GOES 6.7 μm channel: Method and climatology for July 1987, *J. Geophys. Res.*, **98**, 16,669–16,688.
- Soden, B. J., and J. R. Lanzante (1996), An assessment of satellite and radiosonde climatologies of upper tropospheric water vapor, *J. Clim.*, **9**, 1235–1250.
- Soden, B. J., S. A. Ackerman, D. O' C. Starr, S. H. Melfi, and R. A. Ferrare (1994), Comparison of upper tropospheric water vapor from GOES, Raman lidar, and CLASS sonde measurements, *J. Geophys. Res.*, **99**, 21,005–21,016.
- Soden, B. J., et al. (2000), A comparison of radiation codes for retrieving upper tropospheric humidity in the 6.3 μm band: Results from the first GVAP workshop, *Bull. Am. Meteorol. Soc.*, **81**, 797–808.
- Soden, B. J., et al. (2002), Satellite-based assessment of upper tropospheric water vapor measurements during AFWEX, paper presented at Twelfth ARM Science Team Meeting, U.S. Dep. of Energy, St. Petersburg, Fla., 8–12 April.
- Spencer, R. W., and W. D. Braswell (1997), How dry is the tropical free troposphere? Implications for global warming theory, *Bull. Am. Meteorol. Soc.*, **78**, 1097–1106.
- Stephens, G. L., D. L. Jackson, and I. Wittmeyer (1996), Global observations of upper tropospheric water vapor derived from TOVS radiance data, *J. Clim.*, **9**, 305–326.
- Turner, D. D., and J. E. M. Goldsmith (1999), Twenty-four-hour Raman lidar measurements during the Atmospheric Radiation Measurement Program's 1996 and 1997 water vapor intensive observation periods, *J. Atmos. Oceanic Technol.*, **16**, 1062–1076.

- Turner, D. D., R. A. Ferrare, L. A. Heilman Brasseur, W. F. Feltz, and T. P. Tooman (2002), Automated retrievals of water vapor and aerosol profiles from an operational Raman lidar, *J. Atmos. Oceanic Technol.*, *19*, 37–50.
- Turner, D. D., B. M. Lesht, S. A. Clough, J. C. Liljegren, H. E. Revercomb, and D. C. Tobin (2003), Dry bias and variability in Vaisala radiosondes: The ARM experience, *J. Atmos. Oceanic Technol.*, *20*, 117–132.
- Udelhofen, P. M., and D. L. Hartmann (1995), Influence of tropical cloud systems on the relative humidity in the upper troposphere, *J. Geophys. Res.*, *100*, 7423–7440.
- Wang, J., H. L. Cole, D. J. Carlson, E. R. Miller, K. Beirle, A. Paukkunen, and T. K. Laine (2002), Corrections of humidity measurement errors from the Vaisala RS80 radiosonde-application to TOGA-COARE data, *J. Atmos. Oceanic Technol.*, *19*, 981–1002.
- Whiteman, D. N. (2003a), Examination of the traditional Raman lidar technique. I: Evaluating the temperature-dependent lidar equations, *Appl. Opt.*, *42*, 2571–2592.
- Whiteman, D. N. (2003b), Examination of the traditional Raman lidar technique. II: Evaluating the ratios for water vapor and aerosols, *Appl. Opt.*, *42*, 2593–2652.
-
- B. M. Lesht, Environmental Research Division, Argonne National Laboratory, 9700 S. Cass Avenue, Argonne, IL 60439, USA. (bmlesht@anl.gov)
- L. M. Miloshevich, National Center for Atmospheric Research, 1850 Table Mesa Drive, P. O. Box 3000, Boulder, CO 80307-3000, USA. (milo@oak.mmm.ucar.edu)
- B. J. Soden, Geophysical Fluid Dynamics Laboratory, National Oceanic and Atmospheric Administration, P. O. Box 308, Princeton, NJ 08542, USA. (bjs@gfdl.gov)
- D. D. Turner, Cooperative Institute for Meteorological Satellite Studies, University of Wisconsin-Madison, 1225 W. Dayton Street, Madison, WI 53706, USA. (dturner@ssec.wisc.edu)